RESEARCH ARTICLE | MAY 02 2024

Abrupt ternary III–V metamorphic buffers

Thomas G. Farinha ; Edwin Supple ; Brian P. Gorman ; Christopher J. K. Richardson

J. Appl. Phys. 135, 175304 (2024)
https://doi.org/10.1063/5.0203835

Journal of Applied Physics ARTICLE pubs.aip.org/aip/jap

Abrupt ternary III–V metamorphic buffers

Cite as: J. Appl. Phys. **135**, 175304 (2024); doi: 10.1063/5.0203835
Submitted: 16 February 2024 · Accepted: 9 April 2024 ·
Published Online: 2 May 2024

Thomas G. Farinha,[1,2,a)] Edwin Supple,[3] Brian P. Gorman,[3] and Christopher J. K. Richardson[1,2]

AFFILIATIONS

[1]Laboratory for Physical Sciences, University of Maryland, College Park, Maryland 20740, USA
[2]Department of Materials Science and Engineering, University of Maryland, College Park, Maryland 20742, USA
[3]Department of Metallurgical and Materials Engineering, Colorado School of Mines, Golden, Colorado 80401, USA

[a)]**Author to whom correspondence should be addressed:** tfarinha@umd.edu

ABSTRACT

Emerging quantum materials as well as novel traditional electronic and photonic materials may enable a new generation of information science devices if they can be synthesized on suitable substrates. Additionally, material and device designs may benefit from tunable properties through engineered epitaxial strain for the manipulation of the electronic character. In this work, three series of III–V ternary alloys, GaInSb, AlInSb, and InAsSb, are grown via molecular beam epitaxy on GaAs (001) substrates to explore the flexibility of abrupt metamorphic epitaxial layers with tunable lattice parameters between 6.135 and 6.479 Å. Their deposition on both homomorphic GaAs and pseudomorphic AlAs buffers is also explored. The structures of these alloys are characterized via reflection high-energy electron diffraction, high-resolution x-ray diffraction, atomic force microscopy, and transmission electron microscopy to assess their suitability as stable buffer layers with wide variability of accessible lattice parameters.

I. INTRODUCTION

Semiconductor substrates with engineered bandgaps and lattice parameters have been desired for decades to enable next-generation electronic and photonic devices.[1] Additionally, emerging quantum materials are sensitive to substrate selection for thermodynamic and fabrication compatibility as well as electronic functionality. Three-five compounds have a wide range of potential lattice parameters for lattice-matched overlayer engineering, as well as a significant selection of bandgaps, dielectric constants, and effective carrier masses.[2] They are technically important and well known for their use in lasers,[3] hot-carrier solar cells,[4] high-mobility transistors,[5] quantum devices,[6] and buffer layers for emerging quantum materials.[7–9] To date, bulk crystal growth techniques have yet to be successful in creating single crystal ternary III–V substrates without significant cracking or phase separation.[1]

Metamorphic epitaxial heterostructures have been realized with the use of compositionally graded, stepped, and abrupt buffer layers to enable virtual substrates where the lattice constant of the device active region is different than that of the substrate.[10] The key to producing functioning metamorphic epitaxy devices is to engineer high densities of dislocations in regions of the material that do not negatively impact performance. Examples include InAsSb/AlInAsSb heterostructures for infrared LEDs,[11] mid-infrared lasers,[12] superconducting aluminum and titanium nitride microwave resonators,[13,14] and Josephson junctions for superconducting qubits.[15] Metamorphic buffers have also been used in Al/GaSb and Al/AlSb[16] heterostructures to combine superconducting layers with two-dimensional electron gases for superconductor–semiconductor quantum devices.[17]

There are several concerns associated with metamorphic growth implementations. The three most significant are thermodynamic stability, antiphase boundaries, and elevated threading dislocation density (TDD). Previous reports of ternary antimonide alloys tend to target compositions away from balanced constituents, such as $Al_{0.5}In_{0.5}Sb$, to avoid compositions with the greatest likelihood of spinodal decomposition. Antiphase boundaries occur when polar films are grown on non-polar substrates and can be avoided through the selection of substrate orientation[18] and surface preparation.[19] Graded virtual substrates have been most successful in SiGe,[20] with additional success for some III–V alloys using stepped or graded buffers[21–24] to minimize threading dislocation densities and rough surfaces.[11,25–27]

In this article, we investigate the III–V ternary alloys GaInSb, AlInSb, and InAsSb across their full compositional ranges to enable

continuous, deterministic tuning of the lattice parameter from 6.135 to 6.479 Å.[2] The availability of these three alloys with similar variability in lattice parameters offers an additional selection in terms of bandgap and thermodynamic properties that may be important when considering the stability and interfacial behavior of subsequent lattice-matched overlayer growth. It is important to note that this range of lattice parameters is particularly promising to support emerging topological materials. Some examples of quantum materials with in-plane lattice parameters covered in the experimental alloying ranges include Cd_3As_2,[28] SnTe,[29] and HgTe.[30] In addition, III–V quantum wells are promising candidates for hosting topological states.[31–33]

The focus of this work is the experimental demonstration of the thermodynamic stability of three ternary III–V alloy systems across the entirety of their compositional ranges. The samples are grown on GaAs substrates to suppress antiphase boundaries, and threading dislocation densities are evaluated but not optimized. Samples are characterized with High-Resolution X-ray Diffraction (HRXRD), Atomic Force Microscopy (AFM), and Transmission Electron Microscopy (TEM).

II. THERMODYNAMIC CONSIDERATIONS

While group-III-antimonide ternary alloys present opportunities for the lattice-matched growth of overlayers with a range of lattice parameters, the perceived instability of these alloys synthesized using traditional MBE growth temperatures and fluxes needs to be addressed. Calculations of ternary stability are, therefore, accomplished with the solid-state delta lattice parameter (DLP) model[34,35] to account for Gibbs free energy, $\Delta G = \Delta H - T\Delta S + \Omega$, and its dependence on the internal strain parameter, Ω, enthalpy, H, entropy, S, and temperature, T. Thermodynamic properties for arsenides[36] and antimonides[37] are applied to GaInSb, AlInSb, and InAsSb using this DLP model. Calculations suggest that all three of these alloys retain their negative (exothermic) energies of fusion under group-V overpressure at the experimentally demonstrated growth temperatures. Despite the thermodynamic stability of these alloys, they may still undergo phase separation at low temperatures due to spinodal decomposition or at high temperatures via thermal decomposition. Literature-based calculations for the potential miscibility gaps of the experimental III–V ternary alloys suggest that once coherency strain is considered, spinodal decomposition occurs for these alloys at substrate temperatures lower than those typically used during growth.[38] Furthermore, any local interfacial strain between the ternary layer and pseudomorphic buffer would lower the temperature at which spinodal decomposition begins to occur.[39,40] However, this effect is not expected for the current metamorphic layer design. Figure 1 shows the theoretical spinodal decomposition curves for the three antimonide ternary alloys considered here. The highest calculated spinodal decomposition temperature is for InAsSb alloys at approximately 367 °C.

Thermally driven decomposition through phase separation is a known degradation mechanism, which limits the maximum temperature for III–V compound semiconductor MBE growth. The challenge associated with thermal decomposition is that the lowest temperature associated with any constituent degradation must be considered the upper limit for alloy deposition. For the materials

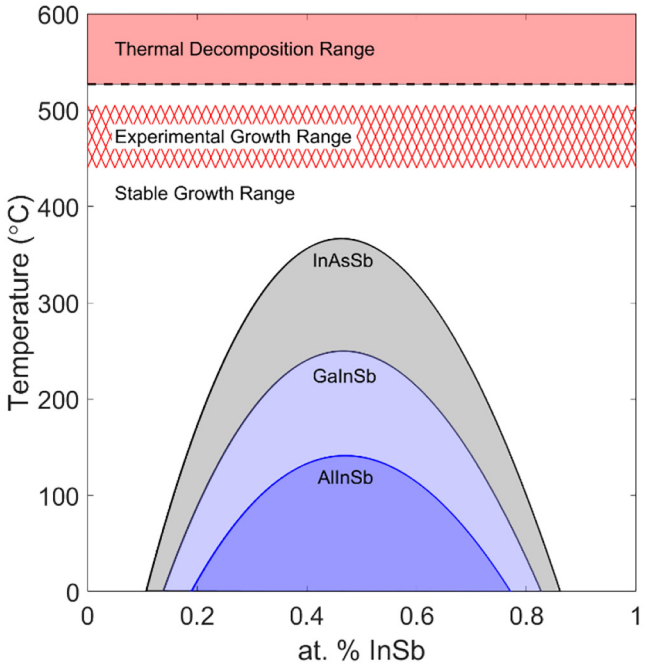

FIG. 1. Calculated III–V ternary alloy spinodal decomposition curves for InAsSb, AlInSb, and GaInSb. The shaded areas below the stability curves demarcate the zones where the respective ternary systems should undergo spinodal decomposition. Also included is the threshold for thermal decomposition in red and the region of stable growth indicated by white space. The experimental growth parameters reside in the stable growth range as indicated by cross-hatching.

evaluated here, the common constituent InSb has the lowest thermal decomposition temperature roughly corresponding to its melting temperature of 527 °C.[1,41] The target growth temperature is, therefore, the range above the alloy-specific spinodal decomposition and below the onset temperature of thermal decomposition at the InSb melting point. This potential growth window is sufficiently wide, offering a minimum range of more than 150 °C.

III. GROWTH AND CHARACTERIZATION

Six variations of III–V metamorphic ternary alloys grown on either homomorphic or pseudomorphic binary buffer layers are explored. All three ternary systems are grown over a range of alloy fractions to investigate the stability of each ternary alloy. Solid source MBE is used to grow all samples reported here. Standard effusion cells produce Ga, Al, and In fluxes, while individual valved effusion cells are used to create As_2 and Sb_2 fluxes using high-temperature crackers. Growth temperatures are achieved through radiative heating and are monitored via infrared pyrometry with the effective emissivity tuned such that the substrate temperature reading during GaAs oxide desorption is 583 °C. Commercial (001)-oriented GaAs wafers with $\lesssim$0.1° offcut are used as the substrate material for all experimental growths.

GaAs oxide desorption is achieved using a 10 min soak at 598 °C under As_2 flux. Both homomorphic GaAs and pseudomorphic AlAs buffers are grown at 560 °C after oxide desorption. A sufficient beam-equivalent pressure V–III ratio is targeted to ensure group-V-rich growth conditions. All samples grown in this report consist of a nominally 300 nm-thick binary arsenide buffer and a 2 μm-thick ternary antimonide overlayer. The use of both GaAs and AlAs buffers explores the potential role of surface energies during the nucleation phase of the metamorphic ternary layers. Antimony overpressure is applied during sample cooldown at the end of each growth until the substrate reaches a pyrometer temperature of 415–425 °C. Antimony flux is chosen to stabilize the surface, and for As–Sb alloys, to prevent group-V exchange according to Gibbs free energy calculations following the DLP model.[42]

Initial growths are focused on exploring the theoretical substrate temperature growth window with a bias toward growing at the maximum temperature that enables the synthesis of homogeneous films. As shown in Fig. 2(a), the substrate temperature markedly increases during the early growth of the ternary overlayer. Growths can be separated into two categories: those that experience a pyrometer temperature, which exceeds the melting temperature of InSb (527 °C) and those that do not. Figure 2(a) shows the pyrometry measurements representing both cases using two samples targeting $Ga_{0.43}In_{0.57}Sb$. Figure 2(b) illustrates the measured HRXRD peaks of the representative samples for both pyrometer cases. Samples grown with a pyrometer temperature that exceeds the melting temperature of InSb decompose into films with a range of lattice spacings including the binary constituents GaSb and InSb. Alternatively, the samples grown with a pyrometer temperature that stays below the melting temperature of InSb result in thin film alloys with a single HRXRD peak and a relatively narrow full width at half maximum (FWHM). As demonstrated by room-temperature HRXRD taken well after ternary layer growth, these films remain stable and single-phase during cooling to room temperature, despite entering their theoretical spinodal decomposition ranges. This is understood to be the result of the kinetic limits of diffusion at such low temperatures.

Pyrometry conducted *in situ* shows a marked increase in the measured sample temperature without any change in the substrate heater power output during the initial growth of all ternary antimonides. The observed increase is the result of two possible effects. A true temperature rise can result from the change in the substrate's heating efficiency during overlayer growth if the new layer has a smaller bandgap than its substrate. This result is expected, as these antimonide layers possess significantly different optical properties in comparison with their arsenide underlayers. Indeed, oscillations in the measured pyrometer temperature, such as in Fig. 3, are observed for some samples as the reflectivity varies as a function of thickness during film growth. Emissivity-corrected pyrometry may be used to mitigate these oscillations and provide for a more accurate assessment of temperature. In addition, an apparent temperature change in the pyrometer temperature can result from the variation in the reflected infrared light that is emitted from the hot effusion cells when shutters are opened or closed, or if the substrate surface

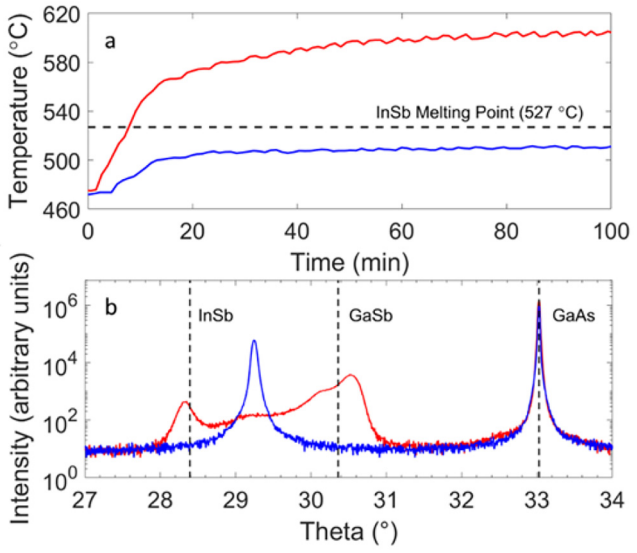

FIG. 2. (a) Pyrometer data for two GaInSb films grown starting with nearly the same growth parameters showing measured increases in the substrate temperature. (b) The XRD plot of a stable $Ga_{0.43}In_{0.57}Sb$ film (blue), as well as the data for a film, which has thermally decomposed after growth temperatures exceeded the InSb melting point of 527 °C (red).

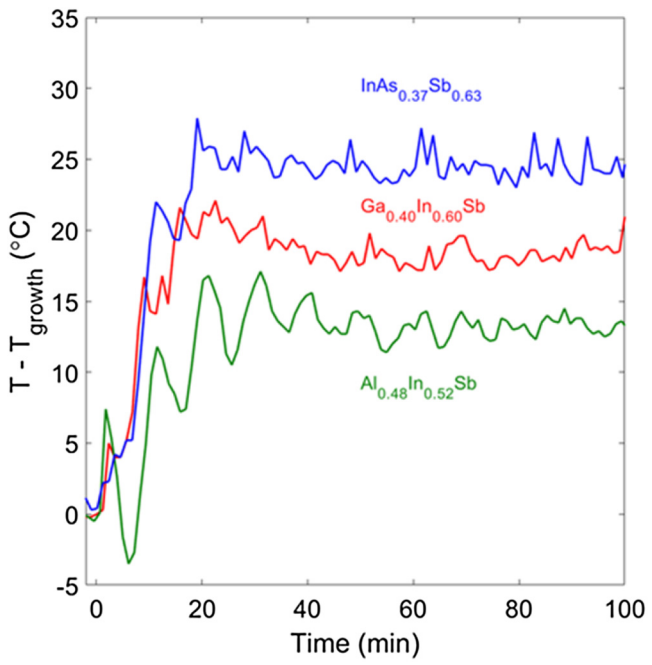

FIG. 3. Measured temperature changes of three samples obtained with pyrometry following the start of growth with the group-III shutters open at time = 0. The temperature shift from the initial setpoint T_{growth} is greater for alloys with larger bandgaps. Signal oscillations appear due to changes in the thickness of the growing film that has different optical properties than the underlying material.

roughness changes. These apparent changes have been negligible during these experiments but are still important considerations.

Reflection high-energy electron diffraction (RHEED) patterns are recorded for each film while at stable growth temperatures and under group-V overpressure. RHEED patterns for three alloys, $Ga_{0.43}In_{0.57}Sb$, $Al_{0.48}In_{0.52}Sb$, and $In_{0.38}As_{0.62}Sb$, are shown in Fig. 4. The common periodicity along sample-specific [110] and [1$\bar{1}$0] directions allows for primary diffraction streak identification. In Fig. 4, the red triangles indicate the primary diffraction streaks that correspond to atomic spacing, the blue triangles indicate clear secondary streaks corresponding to the surface reconstruction for that orientation, and the white triangles indicate faint secondary streaks. All three samples exhibit 3× reconstruction patterns along the [1$\bar{1}$0] direction. The observed GaInSb and AlInSb patterns exhibit 3× RHEED patterns like those of their respective binary antimonides GaSb (1 × 3) or AlSb (1 × 3) at similar growth temperatures.[43,44] For GaInSb and AlInSb, faint secondary streaks along their [110] orientations may be interpreted as the border between the (1 × 3) and (2 × 3) surface reconstructions. The surface reconstruction of InAsSb matches neither its (2 × 4) arsenide[44] nor its pseudo-(1 × 3) antimonide,[45] instead exhibiting a clear (2 × 3) pattern.

HRXRD is used to determine ternary alloy fraction using Vegard's law[46] and the known XRD peak positions of relevant binary III–V constituents.[2] This method of compositional analysis requires that the ternary films be fully relaxed, as strain will move the peaks away from their bulk positions. Figure 5 shows $\omega - 2\theta$ HRXRD data of (004) peaks collected using a four-bounce hybrid Ge (400) monochromator for the Cu-Kα incident beam and a 1/4° acceptance slit in front of a proportional detector for the diffracted beam. Individual data sets are laterally translated to account for slight diffractometer alignment artifacts by using the literature value of the GaAs (004) substrate peak as a common reference. Some samples include an AlAs (004) pseudomorphic buffer peak, which is adjacent to the GaAs (004) peak.

Each of the alloy series and their respective binary endpoints show single diffraction peaks indicating the growth of a homogeneous ternary film. Peaks associated with the ternary alloys are slightly broader and less intense than the AlSb and GaSb endpoints but are narrower and more intense than InAs. The calculated composition and x-ray peak FWHM values for each of these samples are listed in Table I. Vegard's law was used to determine the alloy composition via lattice parameters derived from ternary peak (004) positions. A small satellite peak near 2θ = 64.2° has been inconsistently observed in a variety of samples. This peak is associated with the condensation of metallic antimony on the sample surface due to sub-optimal cooling during the removal of antimony overpressure following growth.

AFM is conducted in the tapping mode, in open air on each sample to monitor variations in the surface topography. The as-grown surfaces for three samples, one from each ternary alloy

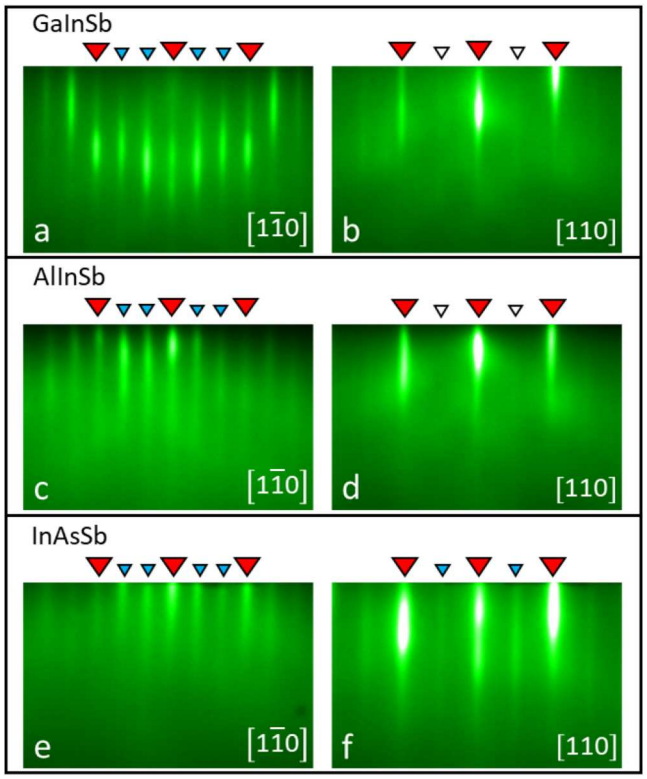

FIG. 4. III–V ternary layer RHEED images corresponding to (a) 3× $Ga_{0.43}In_{0.57}Sb$, (b) 2× $Ga_{0.43}In_{0.57}Sb$, (c) 3× $Al_{0.48}In_{0.52}Sb$, (d) 2× $Al_{0.48}In_{0.52}Sb$, (e) 3× $In_{0.38}As_{0.62}Sb$, and (f) 2× $In_{0.38}As_{0.62}Sb$. Sample-group patterns have a 90° in-plane rotation between them. Red triangles indicate primary diffraction streaks that correspond to atomic spacing, blue triangles indicate clear secondary streaks corresponding to the surface reconstruction for that orientation, and white triangles indicate faint secondary streaks.

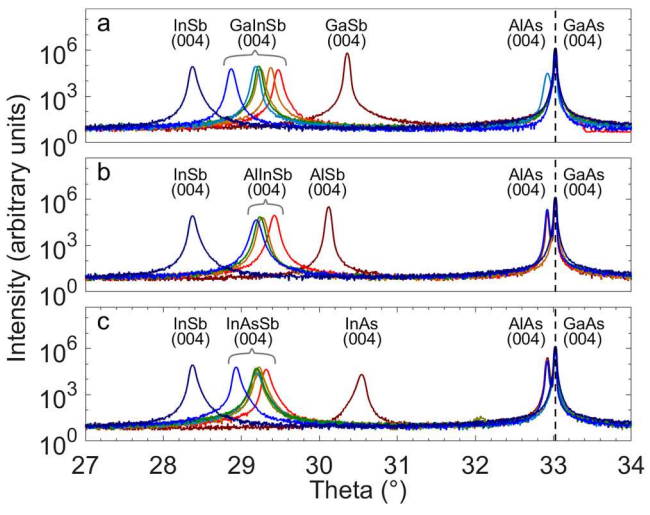

FIG. 5. HRXRD of ternary III–V alloys showing lattice parameter tunability for MBE-grown (a) GaInSb, (b) AlInSb, and (c) InAsSb systems.

TABLE I. Tabulation of growth temperatures, HRXRD (004) peak FWHMs, and AFM RMS roughnesses for all experimental samples shown in Fig. 5.

Alloy	Buffer (300 nm)	Alloy growth temperature (°C)	Alloy (004) peak FWHM (arcsec)	RMS roughness R_q, $10 \times 10\,\mu m^2$ (nm)
$Ga_{56.6}In_{43.4}Sb$	GaAs	473	227	1.85
$Ga_{25.5}In_{74.5}Sb$	GaAs	473	227	3.47
$Ga_{51.6}In_{48.4}Sb$	GaAs	473	205	1.32
$Ga_{45.1}In_{54.9}Sb$	GaAs	473	227	1.54
$Ga_{41.9}In_{58.1}Sb$	AlAs	460	228	5.07
$Ga_{43.9}In_{56.1}Sb$	GaAs	460	207	1.55
$Al_{60.2}In_{39.8}Sb$	AlAs	460	243	3.26
$Al_{46.8}In_{53.2}Sb$	AlAs	460	290	6.89
$Al_{49.8}In_{50.2}Sb$	AlAs	500	255	2.67
$Al_{51.5}In_{48.5}Sb$	GaAs	500	279	3.33
$InAs_{26.3}Sb_{73.7}$	AlAs	460	225	6.40
$InAs_{44.5}Sb_{55.5}$	AlAs	460	249	5.62
$InAs_{38.3}Sb_{61.7}$	AlAs	460	240	2.12
$InAs_{40.1}Sb_{59.9}$	AlAs	440	247	3.89
$InAs_{38.5}Sb_{61.5}$	GaAs	440	332	6.27
$InAs_{40.7}Sb_{59.3}$	GaAs	440	325	11.6
$InAs_{39.0}Sb_{61.0}$	AlAs	440	270	5.50

system, are shown in Fig. 6. First-order plane-fitting and first-order flattening operations were applied to the shown images. The topography of each sample appears to be three dimensional with mounded features and no clear atomic steps. The root-mean-square surface roughness values (R_q) for all ternary alloys shown in Fig. 5 are cataloged in Table I.

Bright-field TEM images viewed along $[01\bar{1}]$ representing the three experimental ternaries are shown in Fig. 7. Samples grown on homomorphic GaAs were chosen to probe the threading dislocation density (TDD) derived exclusively from substrate-ternary mismatch. The imaged samples were prepared by focused ion beam milling and lift-out.[47] A gas injection system was used to deposit a protective coating of Pt. This coating appears as the dark-contrast layer on the left side of all three micrographs. While all three systems exhibit clear threading dislocations running mainly along the {111} planes rotated 45° from the film plane, vertical dislocations that travel along ⟨100⟩ are also apparent. These vertical dislocations are most visible in AlInSb due to the thinness of the lamella. Additionally, there are vertical striations (curtaining) due to sample preparation, which are particularly noticeable in Fig. 7(c). Energy-dispersive x-ray spectroscopy was conducted in the scanning TEM mode but found no evidence of phase separation in these samples. The precision of the utilized parameters is within ±10% composition.

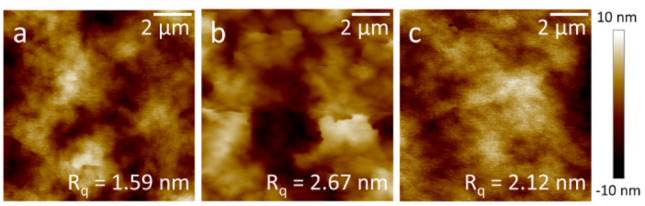

FIG. 6. Representative $10 \times 10\,\mu m^2$ AFM images of the ternary III–V alloys: (a) $Ga_{0.43}In_{0.57}Sb$, (b) $Al_{0.48}In_{0.52}Sb$, and (c) $InAs_{0.36}Sb_{0.64}$. Root-mean-square roughness values (R_q) for each sample are listed in their respective figures.

The TDDs of these samples are counted at their thickness midpoints (50% thickness) and near their surfaces (95% thickness). TDD is estimated by counting dislocations, which cross the plane of measurement, then estimating plane area using the measured width and the lamella depth calculated from the angle of the lamella tilt out of the image plane and projected apparent height of the film/substrate interface. All values are on the order of 10^9 cm^{-2}, and the TDD decreases with buffer thickness. Additionally, the convergent beam electron diffraction pattern observed immediately above and below the film/substrate interface is used to quantify the film mistilt. The mistilt and TDDs are tabulated in Table II.

Reciprocal space maps (RSMs) are conducted using a 2D x-ray sensitive detector set to characterize the symmetric (004) and asymmetric $(\bar{2}\bar{2}4)$ peaks of the experimental samples. They are plotted using the reciprocal lattice unit (rlu), a dimensionless parameter defined as λ/(2d), where λ is the Cu-Kα wavelength and d is the distance between planes belonging to a specific RSM spot. This is done so that the radius of the Ewald sphere $R = 1/2$. The conversions from the goniometer angles, ω and 2θ to the in-plane, Q_x, and out of plane, Q_y, scattering vectors are

$$Q_x = R[\cos\omega - \cos(2\theta - \omega)], \quad (1)$$

$$Q_y = R[\sin\omega + \sin(2\theta - \omega)]. \quad (2)$$

The in-plane lattice parameters of these films are calculated from the measured asymmetric peak d-spacings. Using a low-exit angle geometry, the RSM shown in Fig. 8 is representative of all

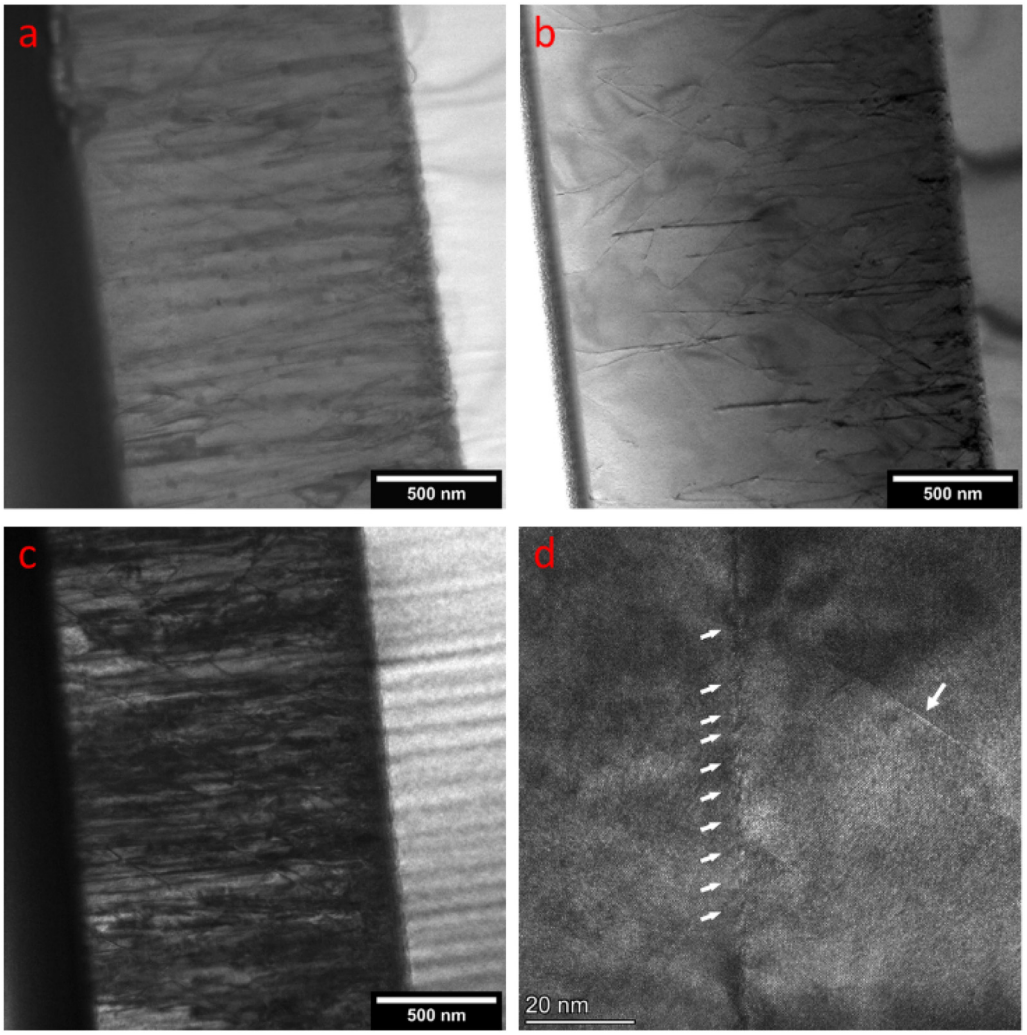

FIG. 7. Bright-field TEM of (a) $Ga_{43.9}In_{56.1}Sb$, (b) $Al_{51.5}In_{48.5}Sb$, and (c) $InAs_{40.7}Sb_{59.3}$ samples used to estimate threading dislocation densities. Threading dislocations appear as dark-contrast streaks in the ternary matrices with visible bend contours near high defect density regions. A high-resolution image of the AlInSb sample (d) demonstrates the presence of both misfit dislocations along the ternary/binary interface and a threading dislocation which travels at a 55° angle with respect to the interface.

three ternary alloy systems. Resultant values in Table III show that all grown films have residual strain below 3×10^{-3}. This confirms that they are relaxed metamorphic films. All data are translated to account for slight ω and θ misalignment artifacts such that the experimental substrate peaks match the positions of the GaAs (004) and ($\bar{2}\bar{2}4$) peaks using literature lattice parameter values.

Further analysis of the ellipticities of the RSM peaks allows for a qualitative measure of relative threading and misfit defect

TABLE II. Threading dislocation densities for three III–V ternaries at both their midpoints and near their surfaces.

Alloy	Film mistilt (001) toward $01\bar{1}$ (degrees)	TDD at 50% thickness (cm^{-2})	TDD at 95% thickness (cm^{-2})
$Ga_{43.9}In_{56.1}Sb$	10	4.27×10^9	3.26×10^9
$Al_{51.5}In_{48.5}Sb$	4	7.16×10^9	2.20×10^9
$InAs_{40.7}Sb_{59.3}$	0	3.57×10^9	2.97×10^9

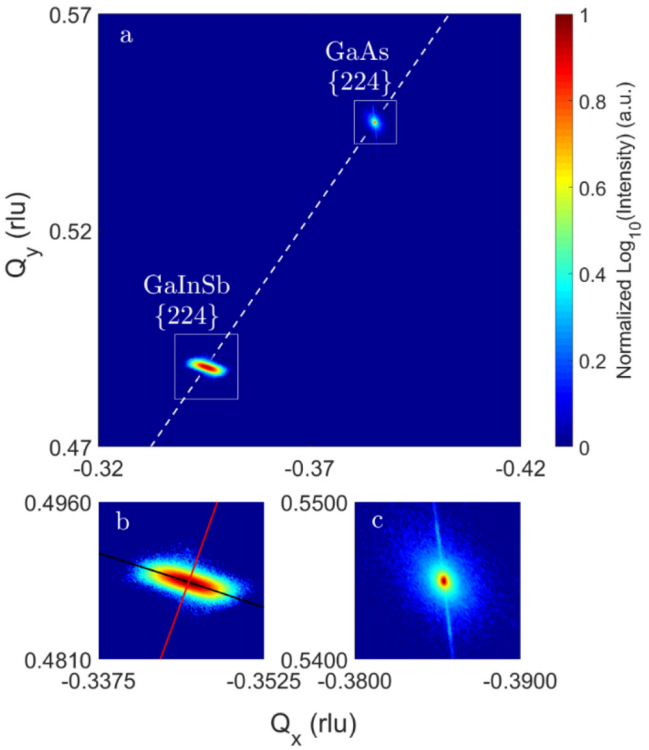

FIG. 8. (a) Reciprocal space map (RSM) of asymmetric GaInSb ($\bar{2}\bar{2}4$) and GaAs ($\bar{2}\bar{2}4$) peaks taken from the same MBE-grown heterostructure. Higher magnification of (b) GaInSb ($\bar{2}\bar{2}4$) and (c) GaAs ($\bar{2}\bar{2}4$) peaks are shown. The black and red lines in (b) are representative of the major axis and minor axis cross sections, respectively.

densities.[48] Specifically, the linear array of misfit (edge) dislocations associated with an ideal abrupt metamorphic interface will produce a (004) RSM spot with an ellipticity that is quantified by the ratio of its major axis FWHM and minor axis FWHM. The FWHM of a 3D Gaussian distribution is $4\sqrt{w \ln 2}$, where w is the width parameter of the specific axis.[42] For metamorphic films that satisfy the requirement $\rho d \gg 1$, the theoretical width parameters for the in-plane (a) and out-of-plane (c) directions are

$$w_a = \rho Q_c^2 b_a^2 / 8\pi d, \tag{3}$$

$$w_c = [\nu/(1-\nu)]^2 \rho Q_c^2 b_a^2 / 4\pi d. \tag{4}$$

The linear dislocation density of the metamorphic layer, $\rho = (a_{film} - a_{sub})/(a_{film} a_{sub})$, is determined from the lattice constants of the film, a_{film}, and substrate, a_{sub}. The film thickness is d, and Q_c is the out-of-plane RSM peak center coordinates in reciprocal lattice units (1/Å). The in-plane Burger's vector b_a is $\langle 110 \rangle$-type with a length of $a/\sqrt{2}$ for zinc-blende III–V crystals.[49] Poisson's ratio, ν, is determined for each unique ternary composition as the linear interpolation of two binary constituent values.

TABLE III. Tabulation of experimental alloy HRXRD-derived in-plane lattice constants (a_{xy}), out-of-plane lattice constants (a_z), in-plane strains (ϵ), experimental and theoretical ellipticities of the RSM (004) peaks, ratios of the experimental and theoretical ellipticity values, direct bandgaps (E_g), and Gibbs free energies at 500 °C ($\Delta G°$).

Alloy	a_{xy} (Å)	a_z (Å)	Strain	Major axis FWHM (rlu)	Experimental ellipticity	Theoretical ellipticity	Ellipticity ratio	E_g (eV)	$\Delta G°$ (kJ/mol)
$Ga_{43.9}In_{56.1}Sb$[a]	6.297	6.311	-1.13×10^{-3}	1.95×10^{-3}	3.660	1.418	2.58	0.31	−18.3
$Ga_{41.9}In_{58.1}Sb$	6.292	6.319	-2.13×10^{-3}	1.53×10^{-3}	2.687	1.413	1.90	0.30	−18.1
$Al_{51.5}In_{48.5}Sb$[a]	6.269	6.302	-2.60×10^{-3}	1.48×10^{-3}	2.131	1.376	1.55	1.14	−28.6
$Al_{49.8}In_{50.2}Sb$	6.273	6.308	-2.76×10^{-3}	1.71×10^{-3}	2.517	1.374	1.83	1.11	−28.1
$InAs_{40.7}Sb_{59.3}$[a]	6.269	6.308	-2.98×10^{-3}	3.92×10^{-3}	4.255	1.314	3.24	0.10	−29.8
$InAs_{39.0}Sb_{61.0}$	6.275	6.315	-3.03×10^{-3}	2.35×10^{-3}	3.217	1.315	2.45	0.10	−29.2

[a]These samples grown on homomorphic GaAs are analyzed via TEM in Table II.

The ellipticity ratio, or ratio of the two axes, provides a thickness independent evaluation of the diffraction spot broadening associated with crystal defects such as threading dislocations, anti-phase boundaries, and phase separation. The experimental ratios ($FWHM_{major}/FWHM_{minor}$) and theoretical misfit FWHM ratios $\left(\sqrt{w_a/w_c}\right)$ for the symmetric (004) RSM peaks are listed in Table III. For each sample, there is a substantial increase in the ellipticity ratio compared to the minimum value anticipated from interfacial misfit dislocations. This increase is consistent with the TEM analysis that found high threading dislocation densities in all samples. The major and minor axis FWHMs have minimum values according to Eqs. (3) and (4), resulting from lattice distortions caused by an array of misfit dislocations. Experimental deviation from these theoretical minima is evidence of other contributions that are often characterized as mosaic spread. Therefore, the major axis FWHM has also been reported for comparison with the literature that may only present results from rocking curve measurements.

Two design parameters, the direct bandgap and Gibbs free energy, are worth cataloging for these samples. The direct bandgap ranges of the three ternary buffer systems offer a significant design space that ranges from 0.10 to 2.27 eV. As shown in Table III, the direct bandgaps are calculated for the reported samples using published bowing parameters.[2] The relative thermodynamic stability of the ternary buffers is important to understand the potential for relative stacking orders of multilayer heterostructures. If lower Gibbs free energy compounds exist using the elements of these III–V ternaries and their neighboring layers, interfacial compounds may form. The Gibbs free energy calculations are, therefore, completed using the DLP model and are cataloged in Table III.

IV. DISCUSSION

The stability of these alloys during growth was the primary concern of this experimental study. It was found that the major obstacle for the growth of the ternary films is the increase in the substrate temperature and possible thermal decomposition associated with the growth of the lower bandgap ternary material that increases the thermal coupling to the radiatively heated substrate. The growth temperature of the overlayer film must also be considered as it pertains to spinodal decomposition. In this regard, there are three distinct temperature ranges. The low-temperature/metastable region corresponds with overlayer growth at a sufficiently low temperature that diffusion is not active and, therefore, the ternary buffer is not in danger of spinodal decomposition during the overlayer growth. In the intermediate temperature region, the overlayer growth is completed within the spinodal decomposition window for the ternary buffer and at sufficient temperatures that diffusion may facilitate the spinodal decomposition of the ternary during overlayer growth. The stable region (used here to grow the ternary buffers) is suitable for overlayer growth being both outside of the spinodal decomposition window and below the thermal decomposition temperature. One example of a potential overlayer for these virtual substrates is Cd_3As_2, which is grown via MBE in the metastable range at approximately 100–200 °C.[7,50,51] Other potential overlayers that are usually grown at higher temperatures, such as Bi_2Se_3 in the range of 300–425 °C,[52] may suffer in quality if spinodal decomposition occurs. In this scenario, the ternaries GaInSb and AlInSb with lower maximum spinodal decomposition temperatures may provide sufficient growth windows to accomplish overlayer growth within the stable region. There does not appear to be any trend matching surface roughness to growth temperature or binary buffer selection. Still, the GaInSb ternaries were the smoothest among the three systems.

The TDD values are high for the reported samples. While these samples are admittedly not suitable for electronic devices, it is important to recognize that they also do not represent the technological limit of low TDD abrupt metamorphic buffers. There is insufficient reporting of similar ternary buffer layers in the literature. It should be noted that high quality MBE quaternary III–V/metamorphic GaSb/GaAs (001) heterostructures have been successfully employed as short-wavelength infrared lasers.[53] For a relative assessment of the level of optimization of the samples, a comparison of the XRD FWHM of the binary endpoints can be made. These values provide insight into the degree of mosaic spread among compared samples of the same system.[54] For the samples reported here, the XRD FWHM of InAs is 259″, GaSb is 173″, AlSb is 169″, and InSb is 220″. Previous reports of the FWHMs of thicker InAs and GaSb metamorphic films taken using a triple-axis analyzer crystal are an order of magnitude narrower.[42]

V. CONCLUSION

This work shows that the ternary III–V alloys, GaInSb, AlInSb, and InAsSb, are stable over a wide range of alloy compositions grown at temperatures ranging from 440 to 500 °C. Thermodynamic analysis and experiments support this growth range as a stable region, which avoids thermal and spinodal decomposition. X-ray diffraction and transmission electron microscopy show that the metamorphic buffer layers are completely relaxed and show no evidence of phase separation. The experimentally confirmed stability of all three alloys over a wide range of compositions confirms them as promising candidates for the lattice-matched MBE growth of novel materials with engineered lattice parameters and physical properties.

AUTHOR DECLARATIONS

Conflict of Interest

The authors have no conflicts to disclose.

Author Contributions

Thomas G. Farinha: Conceptualization (equal); Data curation (equal); Formal analysis (lead); Investigation (lead); Methodology (equal); Software (lead); Validation (lead); Visualization (equal); Writing – original draft (lead); Writing – review & editing (equal). **Edwin Supple:** Conceptualization (supporting); Formal analysis (supporting); Investigation (supporting); Methodology (equal); Validation (supporting); Visualization (supporting); Writing – review & editing (supporting). **Brian P. Gorman:** Conceptualization (supporting); Formal analysis (supporting); Methodology (equal); Project administration (supporting); Resources (equal); Supervision (equal). **Christopher J. K. Richardson:** Conceptualization (equal); Formal analysis (supporting); Funding acquisition (lead); Methodology (equal); Project administration (lead); Resources

(equal); Software (supporting); Supervision (equal); Validation (supporting); Visualization (equal); Writing – original draft (supporting); Writing – review & editing (equal).

DATA AVAILABILITY

The data that support the findings of this study are available within the article.

REFERENCES

[1]P. S. Dutta, in *Springer Handbooks of Crystal Growth*, edited by G. Dhanaraj, K. Byrappa, V. Prasad, and M. Dudley (Springer, Berlin, 2010)), pp. 281–325.
[2]S. Adachi, in *Springer Handbooks*, edited by S. Kasap and P. Capper (Springer International Publishing, Cham, 2017), pp. 725–741.
[3]S. Nakamura, M. Senoh, S. Nagahama, N. Iwasa, T. Yamada, T. Matsushita, H. Kiyoku, and Y. Sugimoto, Jpn. J. Appl. Phys. **35**, L74 (1996).
[4]H. Esmaielpour, K. R. Dorman, D. K. Ferry, T. D. Mishima, M. B. Santos, V. R. Whiteside, and I. R. Sellers, Nat. Energy **5**, 336 (2020).
[5]J. A. del Alamo, Nature **479**, 317 (2011).
[6]J. Shabani, M. Kjaergaard, H. J. Suominen, Y. Kim, F. Nichele, K. Pakrouski, T. Stankevic, R. M. Lutchyn, P. Krogstrup, R. Feidenhans'l, S. Kraemer, C. Nayak, M. Troyer, C. M. Marcus, and C. J. Palmstrøm, Phys. Rev. B **93**, 155402 (2016).
[7]D. A. Kealhofer, H. Kim, T. Schumann, M. Goyal, L. Galletti, and S. Stemmer, Phys. Rev. Mater. **3**, 31201 (2019).
[8]Z. Chen, T. A. Garcia, J. De Jesus, L. Zhao, H. Deng, J. Secor, M. Begliarbekov, L. Krusin-Elbaum, and M. C. Tamargo, J. Electron. Mater. **43**, 909 (2014).
[9]H. Song, J. Yao, Y. Ding, Y. Gu, Y. Deng, M.-H. Lu, H. Lu, and Y.-F. Chen, Adv. Eng. Mater. **21**, 1900410 (2019).
[10]C. J. K. Richardson and M. L. Lee, MRS Bull. **41**, 193 (2016).
[11]G. Belenky, D. Wang, Y. Lin, D. Donetsky, G. Kipshidze, L. Shterengas, D. Westerfeld, W. L. Sarney, and S. P. Svensson, Appl. Phys. Lett. **102**, 111108 (2013).
[12]D. Jung, L. Yu, S. Dev, D. Wasserman, and M. L. Lee, Appl. Phys. Lett. **109**, 211101 (2016).
[13]X.-Y. Liu, I. Arslan, B. W. Arey, J. Hackley, V. Lordi, and C. J. K. Richardson, ACS Nano **12**, 6843 (2018).
[14]C. J. K. Richardson, A. Alexander, C. G. Weddle, B. Arey, and M. Olszta, J. Appl. Phys. **127**, 235302 (2020).
[15]S. Kim, H. Terai, T. Yamashita, W. Qiu, T. Fuse, F. Yoshihara, S. Ashhab, K. Inomata, and K. Semba, Commun. Mater. **2**, 98 (2021).
[16]W. L. Sarney, S. P. Svensson, A. C. Leff, W. F. Schiela, J. O. Yuan, M. C. Dartiailh, W. Mayer, K. S. Wickramasinghe, and J. Shabani, J. Vac. Sci. Technol. B **38**, 32212 (2020).
[17]I. Vurgaftman, J. R. Meyer, and L. R. Ram-Mohan, J. Appl. Phys. **89**, 5815 (2001).
[18]M. Akiyama, Y. Kawarada, and K. Kaminishi, J. Cryst. Growth **68**, 21 (1984).
[19]R. Alcotte, M. Martin, J. Moeyaert, R. Cipro, S. David, F. Bassani, F. Ducroquet, Y. Bogumilowicz, E. Sanchez, Z. Ye, X. Y. Bao, J. B. Pin, and T. Baron, APL Mater. **4**, 046101 (2016).
[20]M. L. Lee, E. A. Fitzgerald, M. T. Bulsara, M. T. Currie, and A. Lochtefeld, J. Appl. Phys. **97**, 11101 (2004).
[21]Y. Jeong, H. Choi, and T. Suzuki, J. Cryst. Growth **301–302**, 235 (2007).
[22]M. K. Hudait, Y. Lin, D. M. Wilt, J. S. Speck, C. A. Tivarus, E. R. Heller, J. P. Pelz, and S. A. Ringel, Appl. Phys. Lett. **82**, 3212 (2003).
[23]S. P. Svensson, W. L. Sarney, D. Donetsky, G. Kipshidze, Y. Lin, L. Shterengas, Y. Xu, and G. Belenky, Appl. Opt. **56**, B58 (2017).
[24]N. J. Quitoriano and E. A. Fitzgerald, J. Appl. Phys. **102**, 033511 (2007).
[25]E. A. Pease, L. R. Dawson, L. G. Vaughn, P. Rotella, and L. F. Lester, J. Appl. Phys. **93**, 3177 (2003).
[26]G. Delhaye, L. Desplanque, and X. Wallart, J. Appl. Phys. **104**, 066105 (2008).
[27]T. Hosoda, D. Wang, G. Kipshidze, W. L. Sarney, L. Shterengas, and G. Belenky, Semicond. Sci. Technol. **27**, 55011 (2012).
[28]M. N. Ali, Q. Gibson, S. Jeon, B. B. Zhou, A. Yazdani, and R. J. Cava, Inorg. Chem. **53**, 4062 (2014).
[29]B. R. Dahal, R. P. Dulal, I. L. Pegg, and J. Philip, Solid State Commun. **253**, 42 (2017).
[30]J. Ruan, S.-K. Jian, H. Yao, H. Zhang, S.-C. Zhang, and D. Xing, Nat. Commun. **7**, 11136 (2016).
[31]W. Mayer, W. F. Schiela, J. Yuan, M. Hatefipour, W. L. Sarney, S. P. Svensson, A. C. Leff, T. Campos, K. S. Wickramasinghe, M. C. Dartiailh, I. Žutić, and J. Shabani, ACS Appl. Electron. Mater. **2**, 2351–2356 (2020).
[32]H. J. Haugan, D. Das, S. Bharadwaj, L. R. Ram-Mohan, J. P. Corbett, R. K. Smith, J. A. Gupta, K. Mahalingam, R. G. Bedford, and K. G. Eyink, Appl. Phys. Lett. **121**, 062109 (2022).
[33]H. Irie, T. Akiho, F. Couëdo, K. Suzuki, K. Onomitsu, and K. Muraki, Phys. Rev. Mater. **4**, 104201 (2020).
[34]G. B. Stringfellow, J. Cryst. Growth **27**, 21 (1974).
[35]L. He, L. E. Clinger, and C. J. K. Richardson, J. Vac. Sci. Technol. B **31**, 061204 (2013).
[36]K. Henke, *Arsenic: Environmental Chemistry, Health Threats and Waste Treatment* (John Wiley & Sons, 2009).
[37]M. E. Schlesinger, Chem. Rev **113**, 8066 (2013).
[38]G. B. Stringfellow, J. Cryst. Growth **65**, 454 (1983).
[39]C. Lin and A. Z. Li, J. Cryst. Growth **203**, 511 (1999).
[40]V. G. Deibuk, Semiconductors **37**, 1151 (2003).
[41]O. Mandelung, *Semiconductors—Basic Data*, 2nd edition (Springer, Berlin, 1996).
[42]C. J. K. Richardson, L. He, and S. Kanakaraju, J. Vac. Sci. Technol. B **29**, 03C126 (2011).
[43]P. M. Thibado, B. R. Bennett, B. V. Shanabrook, and L. J. Whitman, J. Cryst. Growth **175–176**, 317 (1997).
[44]A. S. Bracker, M. J. Yang, B. R. Bennett, J. C. Culbertson, and W. J. Moore, J. Cryst. Growth **220**, 384 (2000).
[45]W. K. Liu and M. B. Santos, Surf. Sci. **319**, 172 (1994).
[46]A. R. Denton and N. W. Ashcroft, Phys. Rev. A **43**, 3161 (1991).
[47]L. A. Giannuzzi and F. A. Stevie, Micron **30**, 197–204 (1999).
[48]V. M. Kaganer, R. Köhler, M. Schmidbauer, R. Opitz, and B. Jenichen, Phys. Rev. B **55**, 1793 (1997).
[49]A. Jasik, I. Sankowska, A. Wawro, J. Ratajczak, R. Jakieła, D. Pierścińska, D. Smoczyński, K. Czuba, and K. Regiński, Appl. Phys. A **124**, 512 (2018).
[50]T. Schumann, M. Goyal, H. Kim, and S. Stemmer, APL Mater. **4**, 126110 (2016).
[51]A. D. Rice, J. Nelson, A. G. Norman, P. Walker, and K. Alberi, ACS Appl. Electron. Mater. **4**, 729 (2022).
[52]Z. Wang and S. Law, Cryst. Growth Des. **21**, 6752 (2021).
[53]P. Apiratikul, L. He, and C.J.K. Richardson, in *CLEO 2013* (Optica Publishing Group, San Jose, CA, 2013), p. CM2K.4.
[54]P. Kidd, P. F. Fewster, and N. L. Andrew, J. Phys. D:. Appl. Phys **28**, A133 (1995).